Selective Vapor Phase Doping of Pt Nanoparticles into Phase-Controlled Nanoalloys

Journal:	*The Journal of Physical Chemistry*
Manuscript ID	jp-2021-10143h.R2
Manuscript Type:	Article
Date Submitted by the Author:	n/a
Complete List of Authors:	Poonkottil, Nithin; Ghent University, Solid state sciences Ramachandran, Ranjith; Universiteit Gent, Department of Solid State Sciences, COCOON Solano, Eduardo; ALBA synchrotron lightsource, Srinath, Nadadur; Ghent University, Laboratory for Chemical Technology Feng, JiYu; Ghent University Faculty of Sciences Werbrouck, Andreas; Ghent University, Department of solid state sciences Van Daele, Michiel; Universiteit Gent, Department of Solid State Sciences Filez, Matthias; Ghent University, Minjauw, Matthias; Universiteit Gent, Department of Solid State Sciences, CoCooN Poelman, Hilde; Universiteit Gent, Laboratory for Chemical Technology Coati, Alessandro; Synchrotron SOLEIL, Detavernier, Christophe; Universiteit Gent, Solid-state Sciences Dendooven, Jolien; Universiteit Gent, Solid State Sciences

Selective Vapor Phase Doping of Pt Nanoparticles into Phase-Controlled Nanoalloys

Nithin Poonkottil†, Ranjith K. Ramachandran†, Eduardo Solano∇, Nadadur Veeraraghavan Srinath‡, Ji-Yu Feng†, Andreas Werbrouck†, Michiel Van Daele†, Matthias Filez†, Matthias M. Minjauw†, Hilde Poelman‡, Alessandro Coati⊥, Christophe Detavernier† and Jolien Dendooven*†

† Conformal Coating of Nanostructures (CoCooN), Department of Solid State Sciences, Ghent Univesity, Krijgslaan 281 (S1), 9000 Ghent, Belgium

‡ Laboratory for Chemical Technology, Ghent University, Technologiepark 125, B-9052 Zwijnaarde, Ghent, Belgium

⊥ Synchrotron SOLEIL, SixS Beamline, L'Orme des Merisiers, Saint-Aubin, BP48, 91192 Gif-sur-Yvette, France

∇ ALBA Synchrotron Light Source, NCD-SWEET beamline, Carrer de la Llum, 2-26, 08290, Cerdanyola del Vallès, Spain

ABSTRACT: Bimetallic nanoparticles (BMNPs) are frontrunners in various fields including heterogeneous catalysis, medicinal applications and imaging. Tailoring their properties requires adequate control over their structure and composition, which still presents a non-trivial endeavour. We present a flexible strategy to deposit phase-controlled BMNPs by vapour phase 'titration' of a secondary metal to a pre-deposited monometallic nanoparticle (NP) host. The strategy is exemplified for archetypal Pt-Sn BMNPs, but transferrable to other BMNPs which alloy noble and non-noble metals. When exposing Pt NPs on a SiO_2 support to discrete TDMASn (tetrakis-(dimethylamino)tin) vapour pulses from 150°C to 300°C, TDMASn selectively decomposes on Pt NPs. This leads to saturated infiltration of Sn into Pt NPs through reactive solid-state diffusion, resulting in the formation of Pt-Sn BMNPs with phase/composition control via the substrate temperature. An additional H_2 pulse after each TDMASn pulse removes the surface ligands and excess Sn on the surface as SnH_4, while preserving the small sizes of the pre-deposited Pt NPs. This approach provides a single step, selective "vapor phase conversion" of Pt NPs into Pt_xSn_y BMNPs with great potential for catalysis. Hereto, a proof of concept is provided by converting wet impregnated Pt NPs into Pt-Sn BMNPs on high surface area supports.

INTRODUCTION

Bimetallic nanoparticles (BMNPs) display superior properties over their monometallic counterparts in applications such as heterogeneous catalysis, nanomedicine[1-3] and magnetism[4-5] as well as imaging.[6] For example, Pt-Sn nanoparticle (NP) catalysts present a model system in catalysis and promote a broad set of targeted chemical transformations in industry, such as propane dehydrogenation into propylene (Oleflex process).[7] The introduction of metallic Sn to Pt can result in improved selectivity towards the desired reaction products compared to monometallic Pt and has therefore been a prototype of performance upgrading by secondary metal addition.[8-13]

Owing to the widespread use of bimetallic NPs in multiple fields, various methods have been developed for tailoring their structure and composition, including impregnation, galvanic displacements, colloidal synthesis and ion exchange.[9, 14-15] As an example, Pt-Sn nanocatalysts can be prepared by coprecipitation or impregnation, but can result in non-uniform, multi-modal size distributions and/or monometallic metal oxide 'impurities', such as SnO_2, aside from the phase pure Pt-Sn nanoalloys. Alternatively, colloidal synthesis provides more accurate control over the NP shape, size, and composition by relying on burst nucleation, but suffers from post-synthesis ligand removal which can result in structural change after controlled synthesis.[9, 16-17]

Atomic Layer Deposition (ALD)[18-19] – on the other hand – is a next-gen, 'gas-phase' alternative for conventional 'liquid-phase' synthesis, as this method allows conformal deposition on 3D surfaces with large surface areas[20,21] and results in volatile by-products which avoids post-deposition cleaning processes after obtaining NPs. In addition, Dendooven et al. demonstrated the excellent capability of ALD to precisely and independently control the size and coverage of Pt nanoparticles.[22]

As a result of the unique features that ALD offers, particularly relevant for catalysis[23-24], there have been successful attempts in literature to deposit bimetallic nanoparticles using ALD. Initially there were reports on the successful deposition of noble metal-based BMNPs, such as Pt-Pd, Pt-Ru, Pd-Ru, based on the area-selective deposition of a second noble metal on a pre-deposited noble metal NP.[25-28] Studies of non-noble metal-based BMNP deposition by ALD have been more scarce due to the non-selective nature of non-noble metal deposition on noble NPs and the difficulty of depositing non-noble metals in their elemental state. Therefore, Ramachandran et al. reported the synthesis of size and phase controlled Pt_xIn_y,[29] Pt_xGa_y[29] and Pt_xSn_y[30] nanoparticles by first depositing a metal oxide layer (In_2O_3, Ga_2O_3 and SnO_2 respectively) followed by metallic deposition of Pt and subsequent temperature programmed reduction (TPR) at high temperature (typically 700°C) to obtain Pt-based BMNPs. This concept was then extended to deposit Pt-Co[31-32], Pt-Zn[33], and Pt-Fe[34] BMNPs. In these works, alloying is thus achieved by a solid-state reaction at high temperature in which the promoting element (Sn, In, …) of the Pt-based bimetallic catalysts is delivered to the Pt from a metal oxide thin film. There are also successful reports on the solid-state formation of alloys through the transport of the alloying element from the support framework to noble metal clusters at the support surface. Pt-Ga BMNPs[35-37] and Pd-Ga intermetallic NPs[38-39] have been synthesized by high-temperature (650°C) reduction of a calcined Ga-modified hydrotalcite-derived support upon which Pt or Pd was impregnated.

Only since recently, Väyrynen *et al.* reported the 'direct' deposition of Co-Sn and Ni-Sn based intermetallic compounds without the need of a bilayered nanocomposite and subsequent TPR.[40] However, these intermetallics are non-noble metal based, and their deposition process alternates Co/Ni ALD with Sn ALD cycles, yielding specific intermetallic stoichiometries. As opposed to this work, we present a low-temperature alloying approach, where the promoting element is selectively 'titrated' to pre-deposited Pt NPs from gas phase. Our synthesis method is exemplified for Pt_xSn_y BMNPs and relies on the selective decomposition of a Sn ALD precursor, tetrakis(dimethyl-amino)tin (TDMASn), on Pt, which induces a solid-state reaction of metallic Sn on the Pt NP surface to form BMNPs at low temperatures. TDMASn is a commonly employed metal-organic precursor in syntheses of ALD films like SnO_2,[41] SnN_x,[42] SnS_x,[43] in molecular deposition of hybrid films like tincone,[44] and in vapor phase infiltration reactions with polymers to generate SnO_2 nanopatterns.[45] Here, we demonstrate its use for the "vapor phase conversion" of Pt NPs into Pt-Sn BMNPs with controllable alloy stoichiometry.

The requirements such a method should meet to be suitable for applications in catalysis can be summarized as: (1) the Sn precursor should selectively interact with the Pt, while leaving the oxide support unchanged, (2) the doping treatment should not induce extensive particle ripening, but preserve the morphology of the original Pt NPs, (3) the amount of inserted Sn atoms should be controllable, and preferably be dependent on only one deposition parameter, and (4) the doping should result in phase-pure nanoalloys rather than mixed phases. In this manuscript, we address all of these aspects, and show that the use of a sequential pulsing sequence comprising TDMASn and H_2 exposures is beneficial compared to exposing the Pt solely to TDMASn vapour in order to meet the morphology requirement and achieve the small particle sizes desired for catalytic applications of the BMNPs. The use of additional H_2 pulses moreover results in a lower, yet controllable, uptake of Sn. To explain these results, the effect of H_2 on the surface chemistry during the doping process is investigated and a mechanism is proposed. Finally, in view of catalytic applications, the stability of the as-synthesized Pt-Sn nanoalloys under reduction-oxidation cycling is also discussed and the applicability of the developed process for the doping of wet impregnated (WI) Pt to Pt-Sn BMNPs on high surface area supports is considered.

Experimental

1. Synthesis of Pt NPs - ALD and wet impregnation

All Pt ALD depositions were performed in a custom-built cold wall ALD chamber with a base pressure of 10^{-6} mbar.[46-47] Pt NPs were prepared by sequentially exposing a SiO_2 surface to trimethyl-(methylcyclopentadienyl)platinum $(MeCp)PtMe_3$ (99 %, Strem Chemicals) and O_2 gas at 300°C.[48] A pre-treatment of three cycles of O_2 plasma (20s) was done prior to each Pt deposition. During both the Pt precursor and O_2 exposure, the pressure in the chamber was ca. 1mbar. For both exposures, a static mode was applied, meaning that the valves to the pumping system were closed during the exposures.

Commercial silica support, SiO_2 (Silica 60 Å pore size Sigma Aldrich) was purchased for the preparation of the supported Pt/SiO_2 catalyst. The loading of Pt on the support was 4 wt% which was prepared by incipient wetness impregnation using an aqueous solution of hexachloroplatinic acid hydrate, $H_2PtCl_6.xH_2O$ (>99.9%, Sigma Aldrich). The material was then subsequently dried at 393 K for 2 h and calcined in air (muffle oven) at 883 K (ramp rate 5 K/min) for 5 hours, yielding the wet impregnated (WI) Pt sample. The BET surface area is determined for the SiO_2 and Pt/SiO_2 samples by means of N_2 adsorption at 77 K (five point method, Tristar Micromeritics) after degassing the sample at 413 K for 5 hours. BET surface area is determined for the SiO_2 and Pt/SiO_2 samples by means of N_2 adsorption at 77 K (five point method, Tristar Micromeritics) after degassing the sample at 413 K for 5 hours.

2. Sn doping

The vapor phase doping was performed in the same ALD reactor as mentioned before. TDMASn was used as a Sn source for all the doping reactions. A typical TDMASn-H_2 cycle consisted of 66s with 6s pulsing time of the precursor, 20s pulsing time of H_2 and 20s pumping time after each pulse. The pressure in the chamber was approximately $6*10^{-3}$mbar during the TDMASn pulse and $2*10^{-2}$ mbar during the H_2 pulse. In between each pulse, the chamber was evacuated to the base pressure. Ar with 99.999 % purity was used as a carrier gas for all precursors.

3. Material and process characterization:

Pt thin film thicknesses were obtained from X-ray reflectivity (XRR) measurements using a Bruker D8

Discover system with Cu Kα radiation. Alternatively, the thickness was extracted with the help of calibrated X-ray fluorescence (XRF) data obtained using a Mo X-ray source (at an angle of 45° with the sample surface) and a silicon drift detector placed at an angle of 52° with the sample surface. For the Pt NPs, the Pt thickness obtained from the XRF-thickness relation should be considered as an equivalent thickness (e.g., 3 nm Pt). The equivalent thickness equals the thickness of a 2D Pt thin film containing the same number of Pt atoms as the real deposited 3D Pt NP morphology. After vapour phase doping, the composition of the Pt-Sn BMNPs was extracted from calibrated XRF measurements (see Supporting Information for details).

In situ XRF and grazing incidence small angle X-ray scattering (GISAXS) measurements during vapour phase doping were performed at the SiXS beamline of the SOLEIL synchrotron, in a dedicated setup for ALD, annealing, plasma and vapour treatments.[49] GISAXS is a powerful method to study the spatial correlation and morphological properties of supported nanoparticles under real processing conditions.[50] The samples were irradiated with 12.0 keV X-rays at an incidence angle of 0.5° for both XRF and GISAXS measurements. The acquisition times were 30 s for XRF and 20 s for GISAXS. The fluorescence spectra were recorded with a Vortex energy-dispersive silicon drift detector. The 2D GISAXS patterns were acquired with a Dectris Eiger 1M detector, positioned at approximately 1.173 m from the sample, with an acquisition time of 60 s. To avoid the possible effect of the X-ray beam on the process and sample, for each measurement a different "fresh" position of the sample was chosen by moving the sample stage. The GISAXS analysis strategy can be found in the Supporting Information.

For gas-phase analysis of reaction products, *in situ* quadrupole mass spectrometry (QMS, Hiden Analytical) was performed using the spectrometer in Multiple Ion Detection (MID) mode with the secondary ion multiplier detector (source voltage 70 V).

SEM measurements after the depositions were performed on a FEI Quanta 200F and a FEI Sirion instrument. Post-deposition annealing treatments of the deposited alloy were performed under different gas atmospheres in a home-built heating chamber mounted on a Bruker D8 diffractometer,[51] enabling in situ X-ray diffraction (XRD) monitoring with Cu Kα radiation. A linear detector covering 20° in 2θ was used to collect the diffracted X-rays with a 2 s time resolution. *Ex situ* GISAXS images of the annealed samples were measured at the NCD-SWEET beamline of the ALBA synchrotron, Spain. The X-ray energy used was 12.4 keV, the incident angle was set at 0.4°, and the sample to detector (Dectris Pilatus 1M) distance was 3 m.

Dark field scanning transmission electron microscopy (STEM DF) was employed for structural analysis after Sn deposition on wet impregnated Pt and Energy Dispersive X-Ray Analysis (EDX) was used as a tool for local chemical analysis. JEOL JEM-2200FS, a Cs-corrected microscope operated at 200kV, equipped with a Schottky-type field-emission gun (FEG) and EDX JEOL JED-2300D was used for all the measurements. The samples were pasted onto a lacey carbon film on a copper grid support.

RESULTS

This section is organized as follows. We first establish the temperature range to accomplish selective decomposition of the Sn precursor on Pt thin films (ca. 10 nm on SiO_2) while avoiding interaction on oxide and nitride surfaces, and demonstrate the doping of Pt thin films to Pt-Sn alloys as a proof of concept, with both TDMASn exposures and an ALD-like sequence of TDMASn and H_2 exposures. Then, we move to Pt NPs on a SiO_2 support, as a relevant model system for catalysis, and address the aspects of particle morphology, Sn uptake and composition/phase control, and phase purity. This is followed by an investigation and discussion on the mechanistic role of H_2. Finally, we discuss the stability of the BMNPs during redox cycling and as a proof of concept, we show that the proposed vapor phase doping strategy can also be employed to convert wet impregnated Pt NPs to Pt-Sn BMNPs on high surface area supports.

Substrate selective decomposition and induced alloy formation

SnO_2 can be deposited via ALD using TDMASn as a precursor up to 325°C on Si (100) without precursor decomposition.[52] However, detailed studies on the decomposition of ALD precursors have been scarce and with limited focus on the potential substrate dependence of the decomposition. Given the importance of this precursor, it is highly desirable to study the substrate dependence of its decomposition behaviour to precisely engineer ALD processes and to tailor potential opportunities for area-selective deposition. Here, we report the decomposition behaviour of TDMASn on different substrates such as sputtered Pt (10 nm), TiN (20 nm), Al_2O_3 (10 nm), and Si with native oxide.

The procedure of performing a decomposition experiment is illustrated in **Figure 1a**, here exemplified for TDMASn. The precursor vapor (TDMASn) is introduced in discrete pulses into the reactor at the desired pressure, separated by a pumping step after each exposure. 30 pulses of TDMASn (15s) at different temperatures were performed and samples were analysed with ex situ XRF to study the decomposition behaviour by checking the extent of Sn deposition. It is worth mentioning that for each temperature range studied, a fresh piece of the substrate is put into the reactor for which the decomposition behaviour was evaluated. Interestingly, the TDMASn precursor decomposed only on the Pt surface in a temperature range of 150°C-300°C, whereas there was no decomposition (no Sn signal from XRF) on the other investigated substrates in this range (**Figure 1b**). Although the precursor starts to decompose on SiO_2 at 350°C, still there was no decomposition on TiN and Al_2O_3. These results clearly indicate that precursor decomposition should not only be considered as a temperature dependent property, but it is also strongly substrate dependent.

The XRD analysis (**Figure 1c**) of the samples with decomposed TDMASn on sputtered Pt revealed the formation of different Pt_xSn_y alloys. For example, at 200°C, there are diffraction peaks arising from PtSn alloy and as the temperature increases the amount of Sn increases on the Pt, which leads to the formation of more Sn rich phases e.g., $PtSn_4$ at 300°C-350°C. The decomposition of TDMASn on Pt versus SiO_2, Al_2O_3 and TiN shows a clear substrate selectivity in the range 150°C-300°C. This phenomenon can be attributed to the reactive nature of the Pt NPs and opens opportunities for area-selective processing on patterned substrates composed of Pt nanostructures on e.g. SiO_2.

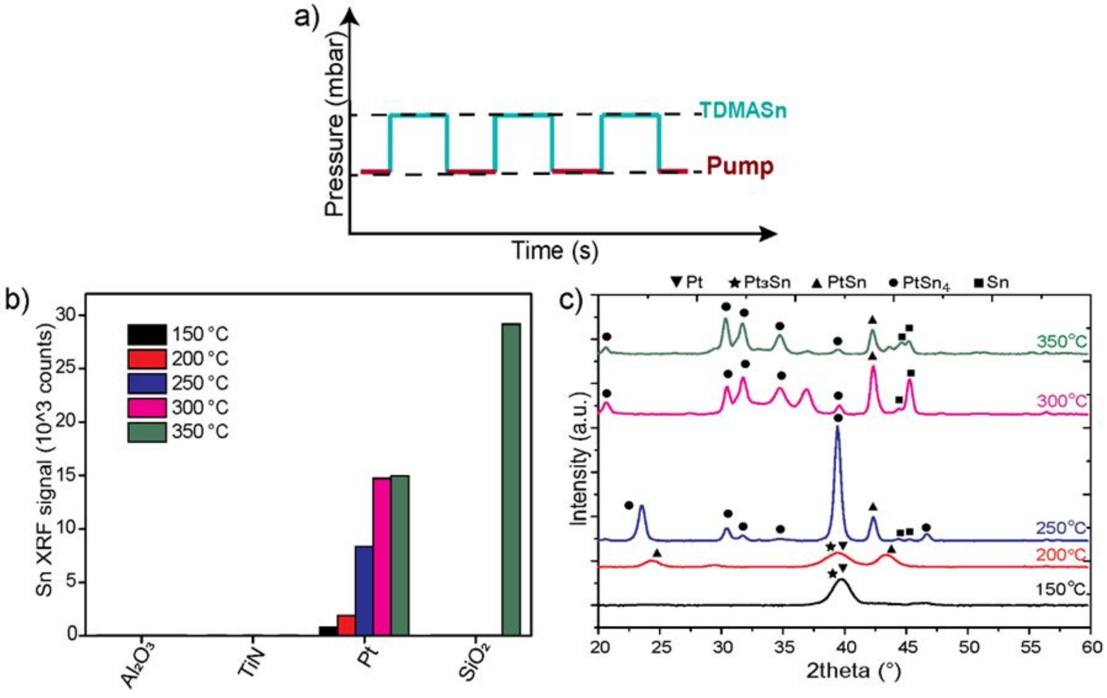

Figure1. a) Schematic representation of a TDMASn decomposition experiment, **b)** Ex situ XRF data (integrated Sn Lα intensity) showing selective decomposition of TDMASn on Pt up to 300°C, **c)** XRD data showing different Pt-Sn bimetallic phases formed after TDMASn decomposition experiments over Pt.

Exposure of PVD Pt to TDMASn vapour at different temperatures resulted in different Pt-Sn bimetallic phases as evident from the XRD results shown in Figure 1c. However, SEM investigation of the samples revealed significantly increased intensity variations after Sn deposition compared to the untreated sputtered Pt layer, pointing towards significant roughening of the surface topography upon TDMASn decomposition and alloying. This is shown in Figure 2c (left vs. middle) for the TDMASn decomposition experiment at 250 °C. Interestingly, introducing intermittent H_2 pulses in the sequence, as indicated in Figure 2a (right), was found to be an effective route towards bimetallic layers with smoother surfaces. Figure 2b (right) and 2c (right) show the XRD pattern and SEM image of the sputtered Pt layer after exposure to 100 cycles of the TDMASn-H_2 process comprising 15s of TDMASn and 20s of H_2, again at a temperature of 250°C. The sequential process resulted in more Pt-rich alloyed phases in XRD than the process using only TDMASn pulses, an observation that was investigated further.

Pt nanoparticle doping

As Pt-Sn BMNPs are potential candidates for catalysis, vapour phase treatments with TDMASn and cyclic TDMASn and H_2 exposures were explored for the doping of Pt NPs. Pt-ALD was used to obtain well-defined Pt nanoparticles, with the (MeCp)$PtMe_3$ and O_2 ALD process[48] at 300°C. The TDMASn only and TDMASn-H_2 treatments were performed at a deposition temperature of 200°C on the Pt NP sample, which had an equivalent thickness of 3 nm. The TDMASn pulse in both processes lasted for 6s and the H_2 pulse for 20s. To get insight in the evolution of Sn uptake, the processes were monitored with in situ XRF. For both processes, after every 5 pulses/cycles both the Sn and Pt XRF signals were collected. The measuring point on the sample was adjusted after each 5 cycles to ensure that the recorded Sn uptake is not influenced by possible effects the X-ray beam may have on the TDMASn decomposition. The XRF counts of Sn and Pt were used to obtain the Sn/(Sn+Pt) atomic ratio in a similar way as reported before[26] (more information is provided in the Supporting Information). As expected, the TDMASn precursor decomposes on the Pt, resulting in an increase in the Sn/(Sn+Pt) atomic ratio (**Figure 3a**). Clearly, the TDMASn only and TDMASn-H_2 processes saturate after reaching a specific amount of Sn on the Pt nanoparticles. However, comparison of the TDMASn only (red dots) and TDMASn-H_2 processes (green dots) reveals that the saturated Sn/(Sn+Pt) atomic ratio for these processes is significantly different. The final ratio for the TDMASn only process is higher (approx. 52%) than for the TDMASn-H_2 process (approx. 25%). Additional *ex situ* XRF experiments at different substrate temperatures indicate that the Sn uptake is systematically higher for the TDMASn only process as shown in **Figure S2**. The Sn/(Sn+Pt) levels at 150°C and 250°C are ca. 28% and 69%, respectively for the TDMASn only process. However, for the TDMASn-H_2 process values of 22% and 46% are found at 150°C and 250°C respectively. This suggests a different reaction mechanism for both processes, where the use of H_2 gas may result in a selective etching of unreacted Sn from the surface. This self-limiting decomposition behaviour opens opportunities towards a highly controllable doping process, similar to the high controllability and conformality that can be obtained thanks to self-limiting surface processes in ALD processing.

The XRD patterns recorded after the two processes are shown in **Figure 3b**. The TDMASn only process leads to the formation of PtSn BMNPs, whereas the TDMASn-H_2 process yields Pt_3Sn BMNPs in agreement with their Sn/(Sn+Pt) atomic ratios.

Particle morphology

For catalytic applications, typically smaller nanoparticles (1-20 nm) are preferred as that would lead to a larger number of active sites (corner atoms, step-edge sites, terrace atoms) for the reaction. The type of site which is effective would depend on the reaction.[53] Therefore, an important question is to what extent the vapor phase doping process is capable of preserving the initial morphology without inducing ripening or coarsening, in particular, for smaller NPs. **Figure 3c, d, and e** show the SEM images of the Pt NPs as deposited, after the TDMASn-H_2doping process and after the TDMASn only process. Inspection of these SEM images clearly reveals a morphological difference between the two processes. While the shape and size of the Pt nanoparticles and the Pt-Sn BMNPs after the TDMASn-H_2 process are similar, the SEM image of the BMNPs obtained with the TDMASn only process clearly demonstrates non-uniform particle shapes and larger particle sizes. In line with the SEM images shown in Figure 2 for Pt thin films, the TDMASn-H_2 process is found beneficial in preserving the original Pt morphology.

The morphological evolution during both processes was studied in more detail with *in situ* GISAXS measurements. The GISAXS images after 20 cycles of both processes are provided in **Figure 4** for easy comparison. Comparison of the GISAXS image of the starting Pt NPs (**Figure 4a**) with the one of the TDMASn-H_2 process (**Figure 4b**) and the TDMASn only process (**Figure 4c**) confirms significant

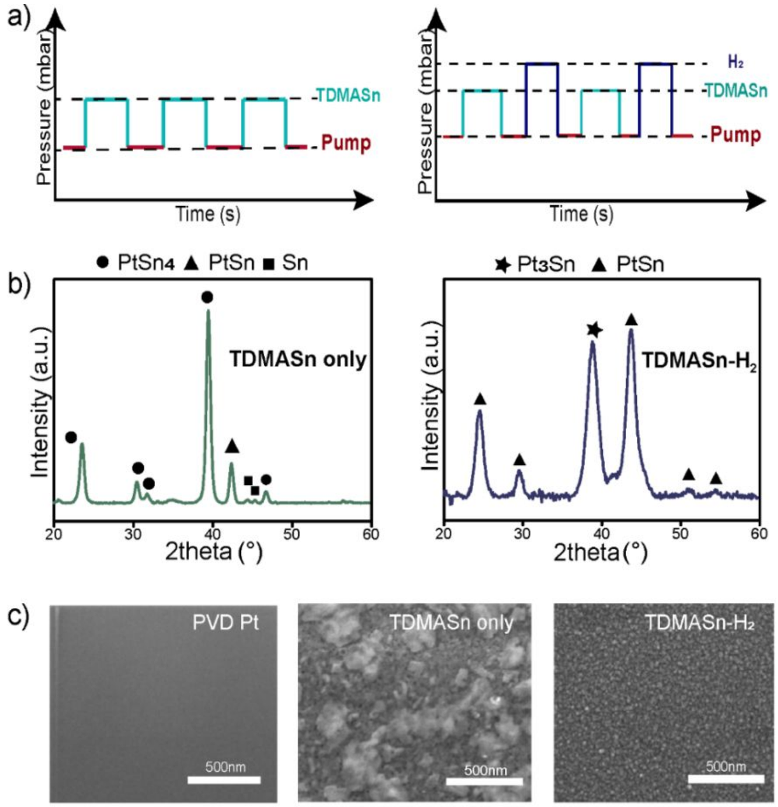

Figure 2. a) Schematic representation of TDMASn 'only' (left) versus alternating TDMASn-H_2 exposures (right), **b)** XRD taken after 30 TDMASn pulses (left) and 100 cycles of the TDMASn-H_2 process (right), both at 250 °C, **c)** SEM images of sputtered Pt film, after TDMASn only process, and after the TDMASn-H_2 process.

differences in the morphological evolution during the doping processes. The Pt and Pt-Sn nanoparticles give rise to a clear scattering peak in GISAXS at $q_y \neq 0$ nm^{-1}.[22] The position of this peak along q_y contains information on the center-to-center interparticle distance (D), which in turn is inversely related to the nanoparticle areal density or coverage. Hence, a shift of the scattering peak to lower q_y values points to an increase in distance and a decrease in particle coverage. This effect would thus be expected if particle coarsening processes occur due to the coalescence and merging of smaller nanoparticles into larger structures. Qualitative inspection of **Figure 4** immediately indicates a clear coarsening effect in case of the TDMASn only process. For this process (**Figure 4c**), the scattering peak has shifted to very low values, which indicates that the interparticle distance has increased considerably during the TDMASn only process and hence the particles are coarsened into large BMNPs.[22, 54-55] In contrast, a close similarity in interparticle distance between the original Pt NPs (**Figure 4a**) and the TDMASn-H$_2$ converted BMNPs (**Figure 4b**) is evident from their GISAXS patterns as the scattering peak remains more or less at the same q_y position.

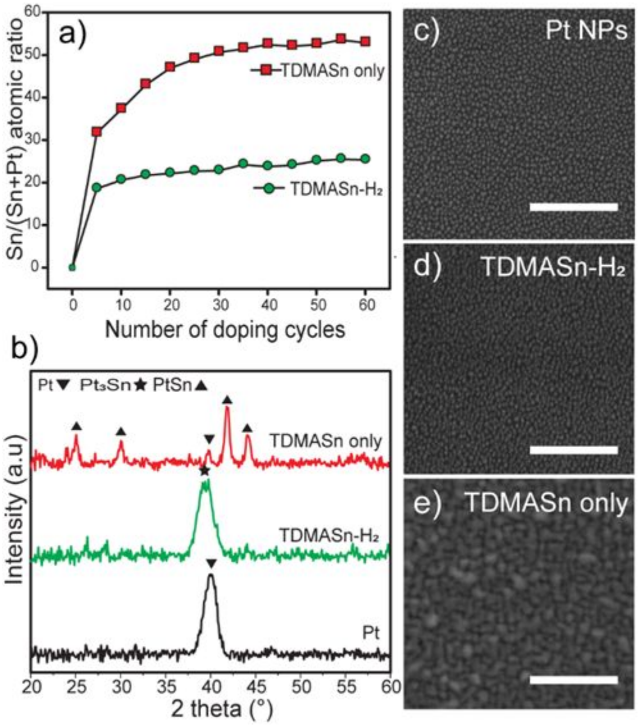

Figure 3. a) In situ XRF data showing the difference in Sn uptake between the TDMASn-H$_2$ and TDMASn only processes. **b)** The XRD patterns of Pt NPs, after 20 cycles of TDMASn-H2 and 20 pulses of TDMASn only processes. **c)**, **d)**, and **e)**. SEM images of the starting Pt NPs (equivalent thickness of 3 nm), the same Pt NPs after 20 cycles of TDMASn-H$_2$ process and 20 pulses of TDMASn only process, respectively. The white scale bars indicate 200 nm.

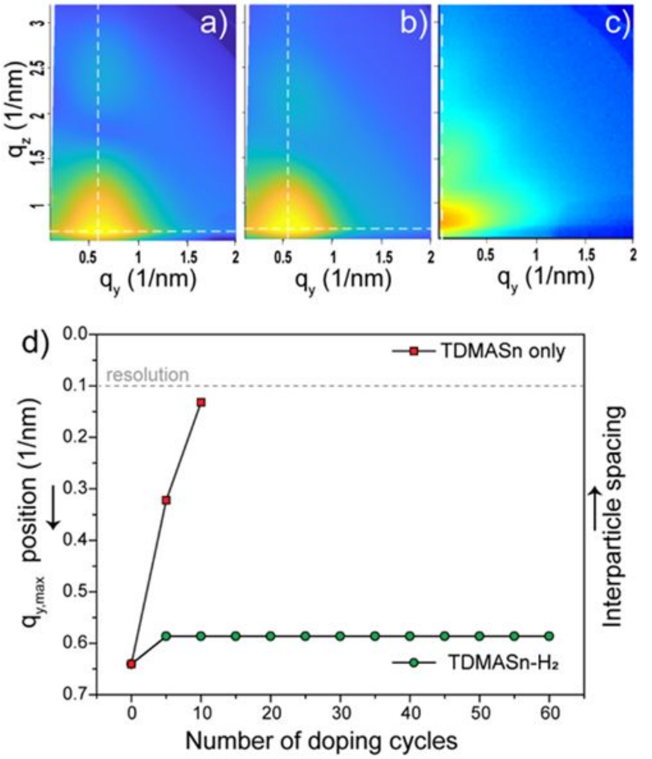

Figure 4. a), b), and c) Recorded GISAXS patterns of Pt NPs as prepared, after the TDMASn-H$_2$ process, and the after TDMASn only process, respectively**.** White dashed lines indicate the q_y maximum position **d)** In situ GISAXS data showing the evolution of the q_y maximum position for the two processes at 200°C. The first data point corresponds to the q_y maximum position of the starting Pt NPs. A decrease in $q_{y,max}$ points to an increase in interparticle spacing as indicated on the right y-axis.

The *in situ* XRF data presented in **Figure 3** showed a clear increase in Sn uptake during the first doping cycles followed by saturation. Importantly, the morphology of the created Pt-Sn BMNPs should also be stable once saturation has been achieved. This is confirmed to be the case by the *in situ* GISAXS patterns that were recorded simultaneously with the XRF spectra (Figure S3). As an illustration, **Figure 4d** shows the q_y position of maximum intensity ($q_{y,max}$), indicated as white dashed lines in (**Figure 4a,b,c**), of each recorded scattering peak. The first data point in the graph corresponds to the bare Pt nanoparticles (starting substrate), for which $q_{y,max}$ was estimated at 0.64 nm^{-1}. After 5 cycles, the $q_{y,max}$ position changes to 0.58 nm^{-1} for the TDMASn-H$_2$ process and then remains stable, in accordance with the saturation behaviour observed in the in situ XRF curve. For the TDMASn only process the $q_{y,max}$ position quickly decreases to values below 0.1 nm^{-1} due to extensive particle coarsening.Finally, the recorded GISAXS patterns after 20 doping cycles were compared with simulated GISAXS patterns (**Figure S4**), obtained using the IsGISAXS software, to extract the average particle width, height and interparticle distance, for the original Pt NPs and the Pt$_3$Sn BMNPs obtained with the TDMASn-H$_2$ process. The reader is directed to the Supporting Information for details on the

GISAXS simulations. The ALD-grown Pt NPs had an average interparticle distance (D) of 8.5 ± 1.3 nm. After the TDMASn-H_2 process, the D value increased slightly to 8.9 ± 1.3 nm. At the same time, the particle width and height of the Pt NPs increased from 5.0 ± 0.8 nm and 4.5 ± 0.3 nm to 6.2 ± 0.9 nm and 5.0 ± 0.4 nm respectively, after the TDMASn-H_2 process. The volume of the Pt NPs thus increases from 59 ± 13 nm^3 to 101 ± 23 nm^3. The theoretical volume increase expected for transforming a face-centred cubic (FCC) Pt NP (JCPDS 04-0802) to FCC Pt_3Sn BMNP (JCPDS 35–1360), calculated based on bulk crystal unit cell parameters, is expected to be around 42 %. Hence, a 60 nm^3 Pt nanoparticle would thus transform to an 85.2 nm^3 Pt_3Sn BMNP.

The fact that well defined nanoparticles are obtained from the TDMASn-H_2 treatment, in a saturated fashion and with negligible NP coarsening, motivated us to explore this process in detail as will be discussed in the next sections.

Sn uptake and composition/phase control

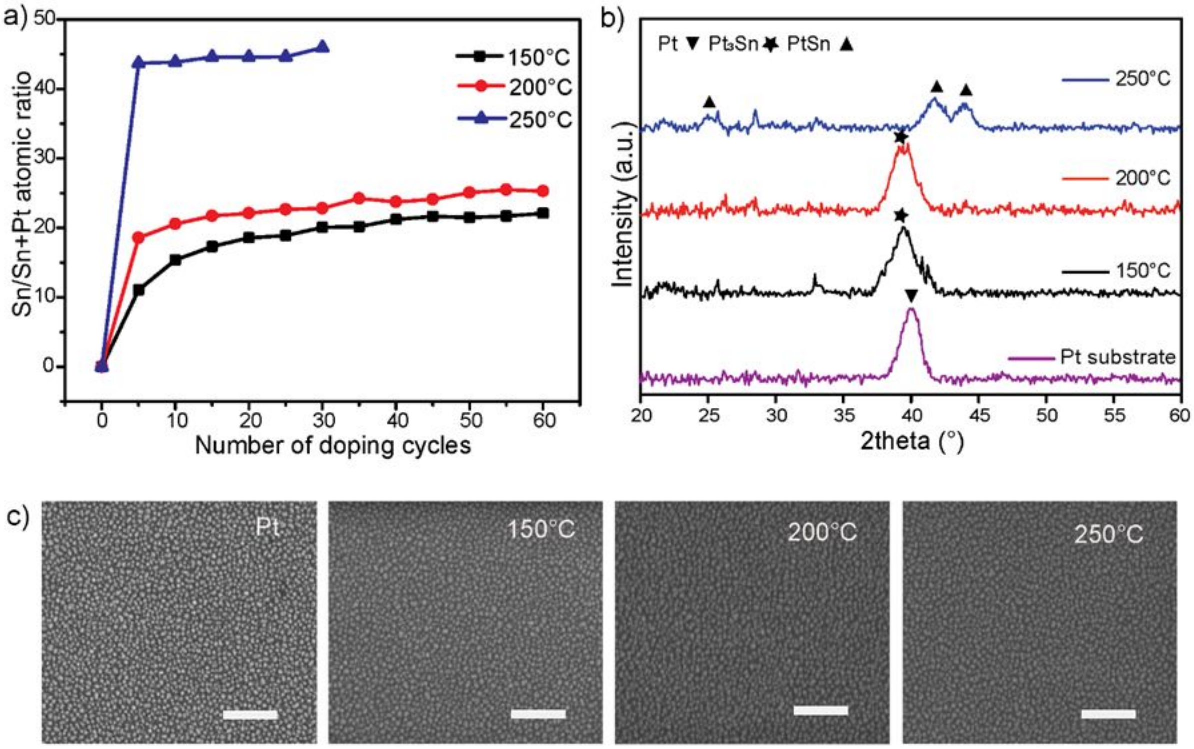

Figure 5. a) *In situ* XRF data showing the variation of Sn/(Sn+Pt) atomic ratio of TDMASn-H_2 process on 3 nm (equivalent thickness) Pt NPs at 150°C, 200°C, and 250°C. **b)** Corresponding XRD data showing the different alloys formed, **c)** The corresponding SEM images, scale bars indicate 100 nm.

Tuning the phase of the BMNPs is important for catalytic applications, as a specific bimetallic phase may be optimal for a specific reaction. Addition of Sn to Pt has, in most cases, shown a positive impact on the performance and/or the stability of the nanoparticles[56-58]. However, in view of activity of the catalyst, higher Sn content is usually not preferred[59-60] and the Sn rich phase $PtSn_4$ is known to be unstable[30] at higher temperature (stable up to only 522°C), where most reactions to be catalysed occur. We used the deposition temperature as a 'tuning knob' to control the phase/composition of the BMNPs. The Sn/(Sn+Pt) ratios at different temperatures were determined, showing a tendency to increase as the temperature increases. The Sn/(Sn+Pt) ratio was ca. 45%, 25%, and 22% at deposition temperatures of 250°C, 200°C, and 150°C, respectively (**Figure 5a**). The figure clearly shows that on Pt NPs of equal loading, the uptake of Sn saturates for all temperatures, but that the amount of Sn added during the TDMASn-H_2 processes increases with the temperature at which the doping is performed.

This opens a way to control the phase/composition of the nanoparticles formed after the TDMASn-H_2 process which is illustrated in **Figure 5b**. The XRD data show a shift of the phase of the Pt-Sn alloy from a Pt rich phase to a less Pt rich phase. More clearly, the diffraction patterns of the BMNPs formed at 150°C and 200°C (2θ=39.2°) suggest the formation of the Pt_3Sn phase. The broadness of the peak is attributed to the diffraction from small nanoparticles, while a contribution of a Pt diffraction peak (2θ=40°) cannot be excluded. At 250°C, a more Sn rich phase, PtSn, can be derived from XRD, in accordance with the higher Sn/(Sn+Pt) atomic ratio of the sample. We restricted our study to the temperatures below or equal to 250°C, as these temperatures will give excellent selectivity of TDMASn towards Pt, while for temperatures above 300°C, some non-selective decomposition on the support may also occur.

The SEM images of the nanoparticles converted at these temperatures were taken to gain insights into their morphology (**Figure 5c**). As expected, they formed BMNPs of well-defined morphology under the temperature range studied.

Effect of Pt loadings on phase purity

The TDMASn-H_2 process turned out to offer an excellent approach to control the phase of Pt-Sn BMNPs with morphologies relevant for catalysis. In this paper, so far, we have already demonstrated the doping of ALD grown Pt NPs with a 3 nm equivalent thickness to Pt-Sn BMNPs. However, for many applications it would be very important to see whether other Pt loadings/thickness can be converted to Pt-Sn BMNPs using the same process. Therefore, different Pt loadings, i.e. with equivalent thicknesses of 3, 7, and 10 nm were prepared by ALD and the TDMASn-H_2 treatment was performed at a deposition temperature of 250°C.

To study the effect of TDMASn-H_2 cycles on the prepared Pt NPs, the number of cycles was varied: 25, 75 and 150 cycles of TDMASn-H_2 process were performed and evaluated with *ex situ* XRF. The Sn/(Sn+Pt) ratio after each deposition was evaluated in a similar way as mentioned earlier and was found to remain almost the same (ca. 48%) for all Pt equivalent thicknesses and also did not change with the number of cycles (**Figure 6a**). The latter indicates that the amount of deposited Sn (inset) did not change even after 150 TDMASn-H_2 cycles on all the Pt NPs which is in agreement with the saturation behaviour shown in **Figure 4**. However, the amount of deposited Sn on the film scales with the Pt thickness, which in turn indicates the saturated doping reaction, where the bimetallic phase is controlled by the temperature and solid-state diffusion behaviour of Sn into Pt, and where excess Sn on the surface is etched away by H_2 (see next section). This leads to a similar (Sn/Sn+Pt) atomic ratio of ca. 48% (expected PtSn phase from the phase diagram) for the three different Pt thicknesses studied.

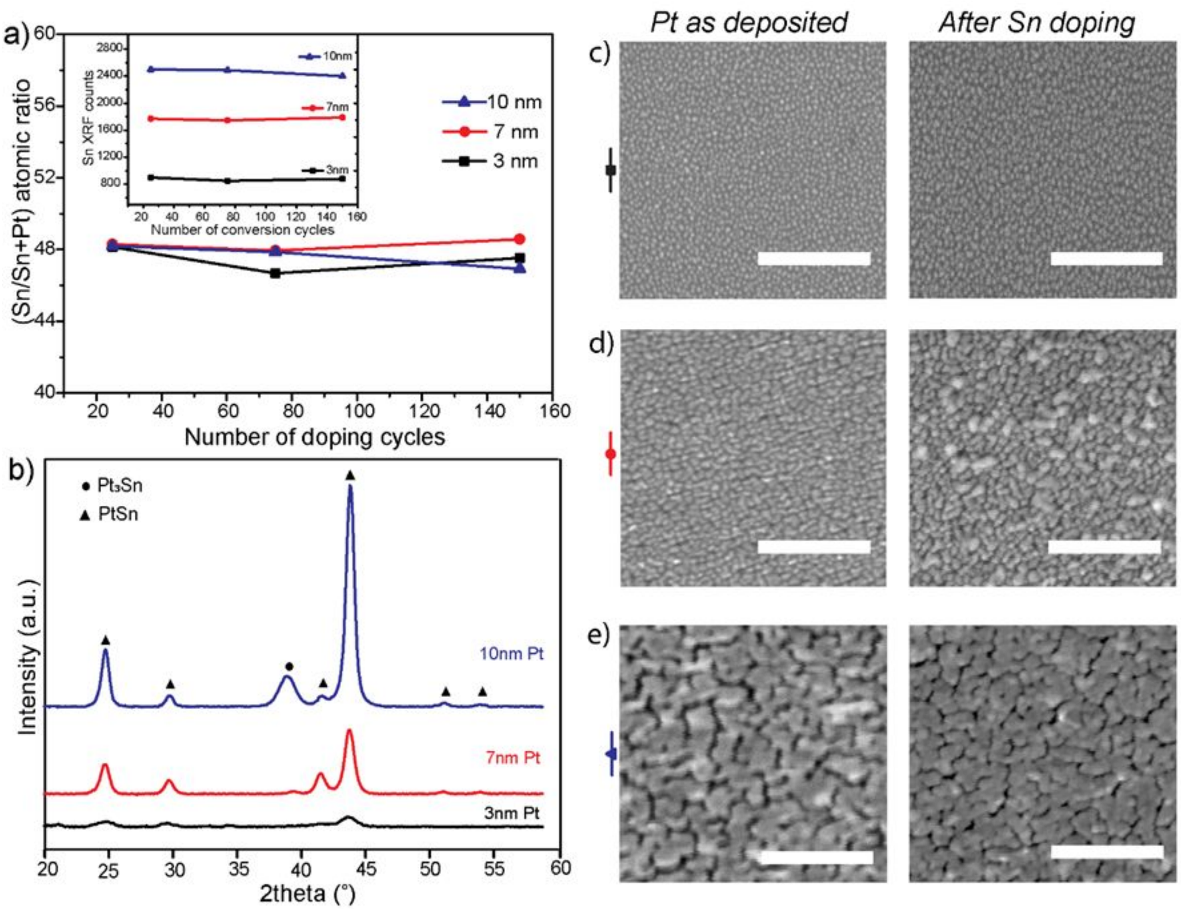

Figure 6. a) Sn/(Sn+Pt) atomic ratio after the TDMASn-H_2 process on different Pt equivalent thicknesses at 250°C. Inset shows *ex situ* Sn XRF counts after the TDMASn-H_2 process. **b)** corresponding XRD patterns. **c)**, **d)**, and **e)** SEM images before and after conversion (150 cycles) for starting Pt NPs of equivalent thicknesses 3 nm, 7 nm, and 10 nm, respectively. The white scale bars indicate 200 nm.

Quite interestingly, the phase formed after the TDMASn-H_2 on all the substrates was confirmed as PtSn except for the 10 nm film on which there was also a diffraction peak arising from Pt_3Sn at ca. 39° (**Figure 6b**). This implies a reactive solid-state diffusion like behaviour for the process, where metallic Sn diffuses into the solid-state Pt NP. Under the conditions studied, at least for films of Pt thicknesses of 7 nm and lower, all Pt is converted into PtSn BMNPs, while for thicknesses equal to or higher than 10 nm, the interaction of Sn with Pt is still ongoing, yet limited by the diffusion of Sn into the Pt matrix as expected for a solid-state reaction. However, this might be mediated by increasing the exposure time or the temperature. The SEM images of the Pt NPs (equivalent thickness of 3 nm, 7 nm, and 10 nm) as deposited and after the TDMASn-H_2 treatment are provided in **Figure 6c-e**.

The role of H_2

The *in situ* XRF data in **Figure 3** revealed a lower deposited Sn amount, when applying an extra H_2 pulse after the TDMASn pulse. The morphological improvement upon using H_2 was shown earlier in **Figure 2, 3 and 4.** The fact that hydrogen radicals (H*) can be used to etch Sn with formation of volatile SnH_4 is well established.[61-62] This effect of hydrogen radicals is in fact being exploited to remove Sn contamination from Extreme Ultraviolet (EUV) mirrors.[61] There are also literature reports showing that atomic hydrogen can etch Sn as SnH_4 from different surfaces.[63]

In our case, for the doping process, we use Pt NPs, which can catalytically split H_2 gas to H* radicals.[28] To evaluate the possible Sn etching as SnH_4, a sample containing both Pt and Sn stripes was prepared on SiO_2 using sputtering (the cross section of such sample is schematically given in the inset in **Figure 7a**). Another sample consisted of a continuous Sn thin film on top of SiO_2 (inset in **Figure 7b**). These samples were exposed to H_2 gas (20 s exposure, 100 pulses) at a substrate temperature of 200°C, in the same conditions and the same reactor as used for the TDMASn-H_2 processes. The amount of Sn before and after the H_2 exposures was again identified by *ex situ* XRF. For the first sample (stripes of Pt and Sn), as shown in **Figure 7a**, a reduction of the Sn XRF counts after H_2 exposure confirms the etching of Sn as SnH_4 on such a sample, facilitated by the formation of H* radicals on the Pt layer. This becomes clear when we observe the Sn XRF counts for the second sample (continuous Sn thin film, **Figure 7b**): there is no significant difference between the Sn XRF counts before and after the H_2 exposures on this sample.

These experiments thus show that Pt enables the splitting of H_2 gas into H* radicals, which subsequently etch Sn with formation of SnH_4 under the conditions of the H_2 exposure step used in the TDMASn-H_2 process. When Pt NPs are used as starting substrate, this may enable even easier splitting of H_2 gas to H* radicals. It is believed that such an etching process is responsible for the lower Sn XRF counts observed for the TDMASn-H_2 process compared to the TDMASn only process (**Figure 3**).

The potential effect of H_2 on removing the ligands from the surface cannot be neglected. To address this hypothesis, mass spectrometry studies were done on 12 nm equivalent thickness Pt NPs prepared by ALD. Both the TDMASn and H_2 pulse lasted for 10s and the deposition temperature used was 200°C. No Sn related fragments were observed during the decomposition of TDMASn performed at different deposition temperatures, possibly due to the high atomic mass of Sn . Hence, SnH_4 or related fragments were not followed using the mass spectrometer, during the TDMASn-H_2 treatment. The significant fragment detected during the decomposition of TDMASn was NCH_3CH_3 (m/z = 44). The evolution of this fragment during the TDMASn only (yellow line in **Figure 7c**) and TDMASn-H_2 (blue line) process was studied. Few cycles of the processes are shown for clarity.

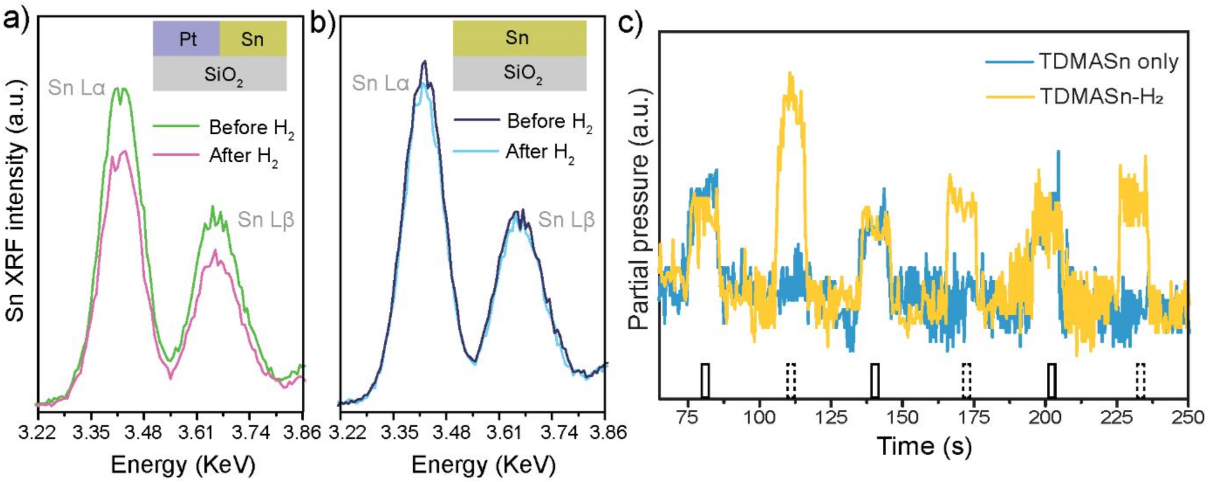

Figure 7. a) and b) *Ex situ* Sn XRF data before and after H_2 pulses for sample containing stripes of Pt as well as Sn and for sample with a continuous Sn thin film (see inset images). c) *In situ* mass spectrometry data for m/z = 44 during the TDMASn only and TDMASn-H_2 process at 200 °C. This may correspond to a NCH_3CH_3 fragment. The solid and dashed vertical bars in the figure correspond to the TDMASn and H_2 pulses, respectively.

From **Figure 7c** it is clear that during each H_2 pulse the removal of the NCH_3CH_3 fragment is observed and the highest release of this fragment is observed during the first H_2 pulse. In fact, the intensity of the peak at m/z = 44 has nearly doubled during the first H_2 pulse when compared to the first TDMASn pulse. This suggests the removal of additional NCH_3CH_3 fragments from the surface by H_2, possibly as $NHCH_3CH_3$. We suspect that the cleaning property of H_2 in removing the ligand fragments from the Pt surface also helps in obtaining a better morphology for the TDMASn-H_2 compared to the TDMASn only process.

Discussion

To summarize the results so far, we demonstrated selective doping of supported Pt NPs into Pt-Sn BMNPs by reactive solid-state diffusion of metallic Sn into Pt NPs. This is achieved in a single step by the selective decomposition of TDMASn precursor on Pt surface. The introduction of an extra H_2 pulse improves the morphology compared to the process without H_2 as evidenced by *in situ* GISAXS and SEM. From the *in situ* XRF data, it followed that the Sn uptake during this process saturates with the number of doping cycles. *In situ* mass spectrometry data showed the removal of organic ligands during the H_2 pulse. The etching of Sn by H_2 was also demonstrated using XRF data.

Figure 8 depicts the mechanistic overview of the TDMASn-H_2 treatment with the results discussed so far. It shows the selective decomposition of the TDMASn precursor on Pt NPs and elemental Sn infiltrating into the Pt NPs forming Pt-Sn based BMNPs. After the TDMASn decomposition on Pt, the surface is left with some excess amount of Sn atoms (in blue) and some ligand fragments. The H_2 exposure etches the loosely bound Sn atoms on the surface as a volatile byproduct SnH_4 and reacts away the NCH_3CH_3 ligands as $NHCH_3CH_3$. This shows the potential of the TDMASn-H_2 treatment as a means to achieve bimetallic nanoparticles with controlled morphology and phase.

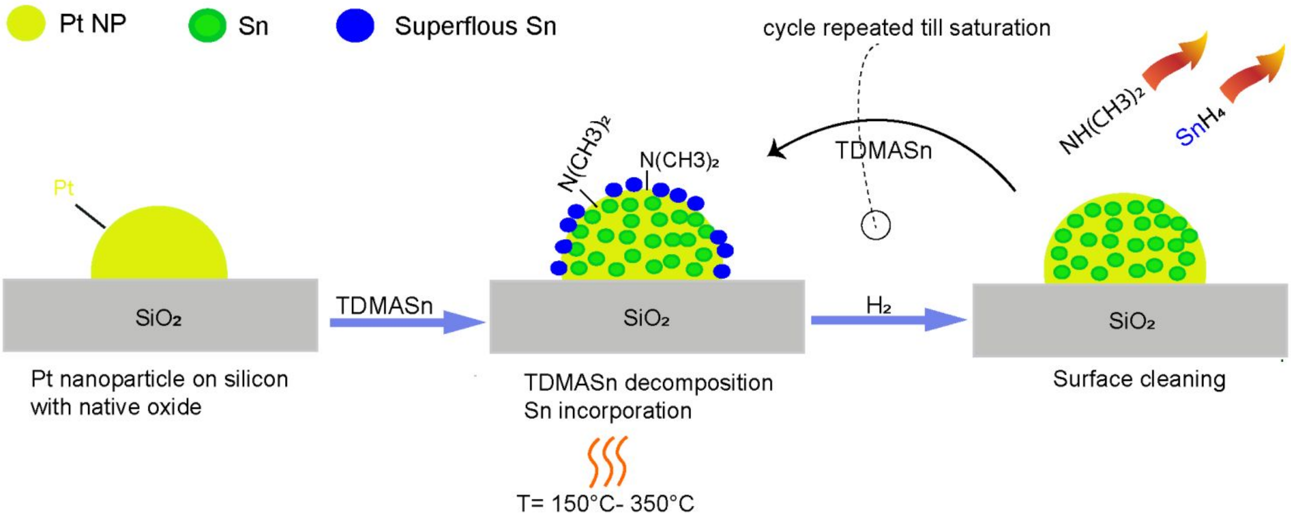

Figure 8. Overall illustration of the TDMASn-H_2 process, a cross-section of a single BMNP is shown for clarity.

Redox behaviour of BMNPs

The behaviour of nanoparticles during a high temperature treatment in different gas atmosphere is very important to evaluate their stability and thereby their activity towards various reactions. In view of catalytic applications or other fundamental studies, the rapid switching behaviour of NPs between different redox states is significant. The importance of this switching behaviour is that coke formed on the NPs can be burnt off to clean the BMNPs and if the BMNPs are oxidized by this process, they can be reduced back to metallic state under H_2 atmosphere.[64-65] Hence, the Pt_3Sn bimetallic nanoparticles prepared by the TDMASn-H_2 process were subjected to annealing treatments in different atmospheres to investigate possible sintering and the morphological evolution at higher temperatures.

XRD measurements after isothermal oxidation/reduction cycling (**Figure 9a**) were done on Pt_3Sn sample prepared at a deposition temperature of 200°C by the TDMASn-H_2 treatment. First, the sample was heated in 20% H_2 in He to 700°C at a ramp rate of 0.2°C/s and after cooling down to room temperature *ex situ* XRD was taken. After this step, the sample was subjected to an O_2 (20% O_2 in He) treatment at 700°C, followed by an *ex situ* XRD measurement after cooldown. This is again repeated for a H_2 treatment of the sample after the O_2 treatment. In between each reduction and oxidation cycle the heating chamber was purged with He to prevent direct mixing of H_2 and O_2. After the H_2 reduction, the diffraction peak at 39.3° (observed for the Pt_3Sn sample as prepared by the TDMASn-H_2 treatment) shifts to lower 2θ angles (39.1°) suggesting the further mixing between Pt and Sn. More interestingly, the peak at

39.1° shifts to the position reported for the Pt (111) diffraction peak (40°) as a consequence of the oxidation treatment. Sn will segregate from the alloy phase and form SnO_2 during this step[59], however, possibly due to its amorphous nature, the diffraction peak corresponding to SnO_2 is not observed. Still, during the next reduction step, the sample is reduced back to Pt_3Sn (39.1°) as evident from the XRD data.

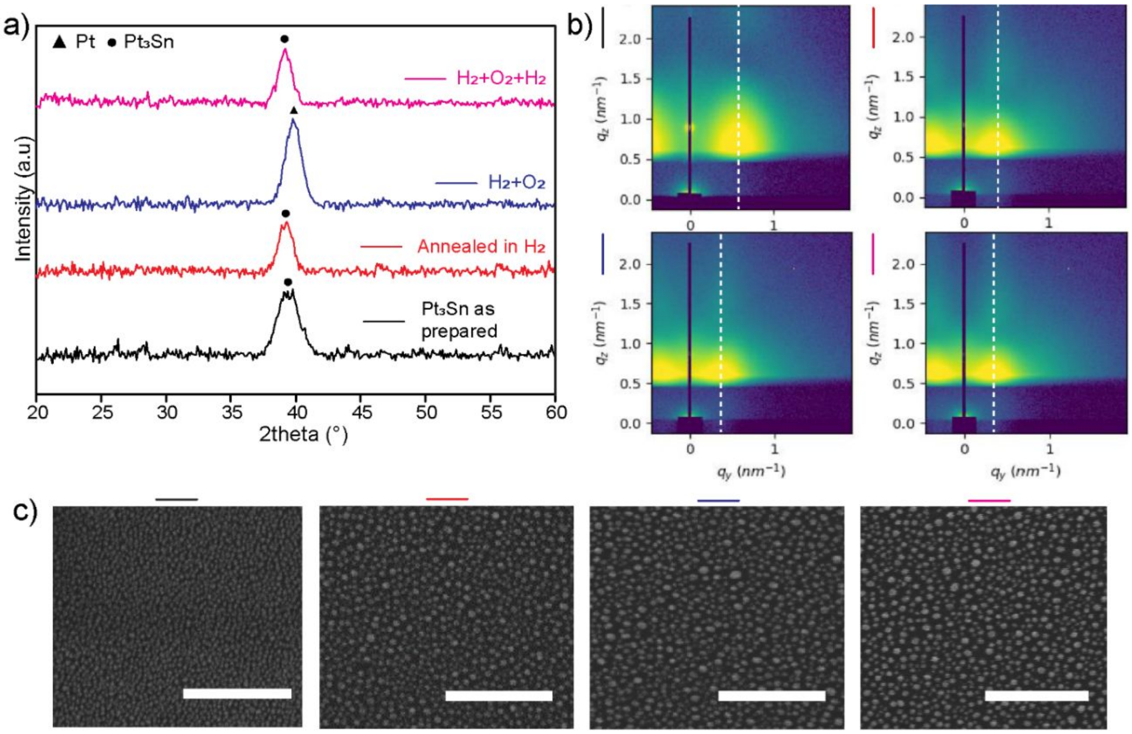

Figure 9. a) *Ex situ* XRD data after treatment in different conditions and cool down, **b)** and **c)** GISAXS and SEM images taken after the treatment in different conditions and cool down, respectively. The white dotted lines in the GISAXS images indicate the q_y maximum position. The white scale bar in SEM corresponds to 200 nm.

The corresponding *ex situ* GISAXS images (**Figure 9b**) and SEM images (**Figure 9c**) allow to assess the possible morphological changes during the high temperature treatment. The scattering pattern for the as prepared Pt_3Sn BMNPs is comparable to the one discussed in Figure 4 ($q_{y,max}$ = 0.58 nm^{-1}). The corresponding SEM image of the Pt_3Sn BMNPs (**Figure 9c** (first image)) is compared with the SEM images after first reduction treatment (second), reduction followed by oxidation (third) and reduction followed by oxidation and further reduction (fourth), indicating some degree of sintering of the BMNPs, which could be expected due to the high particle coverage and thus close proximity of the BMNPs. The BMNP sintering is also evident from the shift in q_y position of maximum intensity to lower values in the GISAXS images recorded after the high temperature treatments, when compared to the image of the as prepared BMNPs.[22, 54]

Doping of WI Pt- proof of concept

As a proof of concept, we also performed the TDMASn-H_2 treatment on wet impregnated (WI) Pt on high surface area SiO_2 support at substrate temperatures of 200°C (**Figure S5**) and 250°C (**Figure S6**). **Figure S6** indicates the STEM image and EDX mapping after the TDMASn-H_2 process (200 cycles) on WI Pt at 250°C. Higher pressure of TDMASn (ca. 2 mbar) was used in this case, in view of uniformly converting the whole Pt/SiO_2 catalyst. After the deposition, the sample was treated in redox atmosphere to around 600°C. The EDX mapping clearly indicates the formation of Pt-Sn alloy with an intensity ratio of almost 1:1, as evident from the EDX line scan.

Also, it is clear from the overlaid image that there is no Sn deposition on the SiO_2 support, rather the Sn is concentrated on the regions where there is Pt, which again demonstrates the selectivity of the doping process, as discussed before. More interestingly, we found that doing the same process on another batch of the same WI Pt/SiO_2 sample at a substrate temperature of 200°C (**Figure S5**), yielded lesser Sn compared to the one at 250 °C, which corroborates our observation that the Sn content on the sample can be controlled by varying the substrate temperature during doping.

CONCLUSIONS and OUTLOOK

Decomposition of ALD precursors is often considered as a temperature dependent property, but through this work we provide proof that decomposition can also be substrate dependent, using TDMASn as an example. The TDMASn precursor decomposes selectively on Pt in a temperature range of 150°C-300°C, whereas no decomposition was observed on other common ALD substrates like SiO_2, Al_2O_3, and TiN as illustrated by the XRF data. This selective decomposition resulted in the formation of Pt_xSn_y alloys. The doping process could be improved by an extra H_2 pulse after each TDMASn pulse, resulting in a cyclic TDMASn-H_2 process.The incorporation of Sn in the Pt NPs shows a saturating behaviour as a function of the number of TDMASn-H_2 doping cycles, while the amount of inserted Sn can be controlled via the deposition temperature. It is found that the H_2 etches superfluous Sn and leaves only the necessary Sn required for the alloy formation. Mass spectrometry provides insights into the removal of precursor fragments from the Pt surface by H_2 as $NHCH_3CH_3$. In situ GISAXS and SEM show that this selective etching of Sn and removal of ligand fragments are crucial for improving the morphology of Pt_xSn_y BMNPs. The introduction of a H_2 pulse helps to avoid agglomeration of the Pt NPs during vapour phase doping and retain the small NP sizes desired for catalytic applications of the BMNPs. Phase-pure alloys are obtained when small Pt NPs are converted (< 7 nm) and phase tuning, i.e. Pt_3Sn versus PtSn, could be accomplished by varying the substrate temperature during the TDMASn-H_2 process from 150°C to 250°C. While a Pt-Sn alloy is formed already after the TDMASn-H_2 treatment at low temperatures, a post-deposition redox cycle at 600 °C is found to further improve the degree of alloying.

This work exemplifies the selective doping process using TDMASn, but this strategy is expected to be applicable to other alkyl amido precursors such as TDMAHf, TEMAV, TDMAGa, TDMAT etc. as these precursors are very similar in structure and may therefore behave in a similar way on a given surface. As an illustration, the results of decomposition experiments of TEMAV on different substrates at substrate temperatures of 150°C, 200°C and 250°C are presented in Figure S8a. It is clear that decomposition of TEMAV already starts at 150°C on a Pt surface, whereas there was no decomposition on other substrates studied. This result is in line with the observations presented for the TDMASn process, providing a hint that in general the 'TDMA' type precursors could be implemented for the selective doping of Hf, V, Ga, Ti etc. into Pt NPs, with potential applications in catalysis. In addition, the approach presented in this study can be extended to other noble metal NPs. For example, Pd could also trigger selective decomposition of similar precursors, and hence the formation of a Pd based nanoalloy. Indeed, exposure of Pd nanoparticles to TDMASn also led to the decomposition of TDMASn as shown in the XRF data presented in Figure S8b. The corresponding XRD patterns in Figure S8c indicate the formation of $PdSn_2$ bimetallic nanoparticles. This shows the generality of our doping approach for different noble metals and alkyl amido precursors. Apart from alkyl amido precursors, other ALD precursors such as those of the diketonate type also have potential for selective vapor phase doping on metal surfaces. For instance, decomposition of tris(2,2,6,6-tetramethyl-3,5-heptanedionato)ruthenium(III) ($Ru(tmhd)_3$) was found to occur on Ni (100) single crystals already at low temperature.[66]

ASSOCIATED CONTENT

Supporting Information

Composition determination from calibrated XRF data, GISAXS analysis strategy, GISAXS simulations of Pt NPs and after TDMASn-H_2 process, extra GISAXS images of TDMASn-H_2 doping process, BET surface area data for WI Pt NPs, TEM data for the doping of WI Pt at a deposition temperature of 200°C.

AUTHOR INFORMATION

Corresponding Author

*Email: Jolien.Dendooven@UGent.be

*Email: Christophe.Detavernier@UGent.be

Conflicts of interest

There are no conflicts of interest to declare.

Author Contributions

The manuscript was written through contributions of all authors.

All authors have given approval to the final version of the manuscript.

Notes

The authors declare no competing financial interest.

ACKNOWLEDGEMENTS

This project has received funding from the European Union's Horizon 2020 research and innovation programme under the Marie Skłodowska-Curie grant agreement no. 765378. The authors would like to thank the beamline staff of SOLEIL synchrotron for smoothly running the facilities. *Ex situ* GISAXS experiments were performed at NCD-SWEET beamline at ALBA Synchrotron with the collaboration of ALBA staff. The authors would like to acknowledge the Flemish Research Foundation (FWO- Vlaanderen), the Special Research Fund BOF of Ghent University (GOA 01G01513) and the CALIPSO Trans National Access Program funded by the European Commission in supplying financing of travel costs.

REFERENCES

1. Chen, W.; Zheng, X.; Li, S.; Zhang, W.; Wen, X.; Yue, L.; Wang, J., One-Pot Synthesis of Fept/Cnts Nanocomposites for Efficient Cellular Imaging and Cancer Therapy. *Journal of Nanoparticle Research* **2015**, *17*, 444.
2. Zhao, Y.; Ye, C.; Liu, W.; Chen, R.; Jiang, X., Tuning the Composition of Aupt Bimetallic

Nanoparticles for Antibacterial Application. *Angewandte Chemie International Edition* **2014**, *53*, 8127-8131.

3. Zheng, X.; Chen, W.; Cui, P.; Wang, Z.; Zhang, W., Design of Multifunctional Fept/Go Nanocomposites for Targeting, Dual-Modal Imaging Diagnostic and in Situ Therapeutic Potential Theranostic Platform. *RSC Advances* **2014**, *4*, 58489-58494.
4. Lyubina, J.; Opahle, I.; Richter, M.; Gutfleisch, O.; Müller, K.-H.; Schultz, L.; Isnard, O., Influence of Composition and Order on the Magnetism of Fe–Pt Alloys: Neutron Powder Diffraction and Theory. *Applied physics letters* **2006**, *89*, 032506.
5. Mustieles Marin, I.; Asensio, J. M.; Chaudret, B., Bimetallic Nanoparticles Associating Noble Metals and First-Row Transition Metals in Catalysis. *ACS Nano* **2021,** *15***,** 3550-3556.
6. Loza, K.; Heggen, M.; Epple, M., Synthesis, Structure, Properties, and Applications of Bimetallic Nanoparticles of Noble Metals. *Advanced Functional Materials* **2020**, *30*, 1909260.
7. Sinfelt, J. H., Structure of Bimetallic Clusters. *Accounts of Chemical Research* **1987**, *20*, 134-139.
8. Liu, L.; Corma, A., Metal Catalysts for Heterogeneous Catalysis: From Single Atoms to Nanoclusters and Nanoparticles. *Chemical reviews* **2018**, *118*, 4981-5079.
9. Toshima, N.; Yonezawa, T., Bimetallic Nanoparticles—Novel Materials for Chemical and Physical Applications. *New Journal of Chemistry* **1998**, *22*, 1179-1201.
10. Franceschetti, A.; Zunger, A., The Inverse Band-Structure Problem of Finding an Atomic Configuration with Given Electronic Properties. *Nature* **1999**, *402*, 60-63.
11. Zaleska-Medynska, A.; Marchelek, M.; Diak, M.; Grabowska, E., Noble Metal-Based Bimetallic Nanoparticles: The Effect of the Structure on the Optical, Catalytic and Photocatalytic Properties. *Advances in colloid and interface science* **2016**, *229*, 80-107.
12. Tao, F. F., Synthesis, Catalysis, Surface Chemistry and Structure of Bimetallic Nanocatalysts. *Chemical Society Reviews* **2012**, *41*, 7977-7979.
13. Filez, M.; Poelman, H.; Redekop, E. A.; Galvita, V. V.; Alexopoulos, K.; Meledina, M.; Ramachandran, R. K.; Dendooven, J.; Detavernier, C.; Van Tendeloo, G.; et al. Kinetics of Lifetime Changes in Bimetallic Nanocatalysts Revealed by Quick X-Ray Absorption Spectroscopy. *Angewandte Chemie International Edition* **2018**, *57*, 12430-12434.
14. Zhao, X.; Yin, M.; Ma, L.; Liang, L.; Liu, C.; Liao, J.; Lu, T.; Xing, W., Recent Advances in Catalysts for Direct Methanol Fuel Cells. *Energy & Environmental Science* **2011**, *4*, 2736-2753.
15. Yang, H., Platinum-Based Electrocatalysts with Core–Shell Nanostructures. *Angewandte Chemie International Edition* **2011**, *50*, 2674-2676.
16. Nasrabadi, H. T.; Abbasi, E.; Davaran, S.; Kouhi, M.; Akbarzadeh, A., Bimetallic Nanoparticles: Preparation, Properties, and Biomedical Applications. *Artificial cells, nanomedicine, and biotechnology* **2016**, *44*, 376-380.
17. Sharma, G.; Kumar, A.; Sharma, S.; Naushad, M.; Dwivedi, R. P.; ALOthman, Z. A.; Mola, G. T., Novel Development of Nanoparticles to Bimetallic Nanoparticles and Their Composites: A Review. *Journal of King Saud University-Science* **2019**, *31*, 257-269.
18. George, S. M., Atomic Layer Deposition: An Overview. *Chemical Reviews* **2010**, *110*, 111-131.
19. Puurunen, R. L., Surface Chemistry of Atomic Layer Deposition: A Case Study for the Trimethylaluminum/Water Process. *Journal of applied physics* **2005**, *97*, 9.
20. Detavernier, C.; Dendooven, J.; Sree, S. P.; Ludwig, K. F.; Martens, J. A., Tailoring Nanoporous Materials by Atomic Layer Deposition. *Chemical Society Reviews* **2011**, *40*, 5242-5253.
21. Cremers, V.; Puurunen, R. L.; Dendooven, J., Conformality in Atomic Layer Deposition: Current Status Overview of Analysis and Modelling. *Applied Physics Reviews* **2019**, *6*, 021302.
22. Dendooven, J.; Ramachandran, R. K.; Solano, E.; Kurttepeli, M.; Geerts, L.; Heremans,

G.; Rongé, J.; Minjauw, M. M.; Dobbelaere, T.; Devloo-Casier, K.; et al. Independent Tuning of Size and Coverage of Supported Pt Nanoparticles Using Atomic Layer Deposition. *Nature communications* **2017**, *8*, 1-12.

23. Lu, J.; Elam, J. W.; Stair, P. C., Synthesis and Stabilization of Supported Metal Catalysts by Atomic Layer Deposition. *Accounts of chemical research* **2013**, *46*, 1806-1815.

24. Lu, J.; Elam, J. W.; Stair, P. C., Atomic Layer Deposition—Sequential Self-Limiting Surface Reactions for Advanced Catalyst "Bottom-up" Synthesis. *Surface Science Reports* **2016**, *71*, 410-472.

25. Cao, K.; Zhu, Q.; Shan, B.; Chen, R., Controlled Synthesis of Pd/Pt Core Shell Nanoparticles Using Area-Selective Atomic Layer Deposition. *Scientific Reports* **2015**, *5*, 8470.

26. Christensen, S. T.; Feng, H.; Libera, J. L.; Guo, N.; Miller, J. T.; Stair, P. C.; Elam, J. W., Supported Ru−Pt Bimetallic Nanoparticle Catalysts Prepared by Atomic Layer Deposition. *Nano Letters* **2010**, *10*, 3047-3051.

27. Lu, J.; Low, K.-B.; Lei, Y.; Libera, J. A.; Nicholls, A.; Stair, P. C.; Elam, J. W., Toward Atomically-Precise Synthesis of Supported Bimetallic Nanoparticles Using Atomic Layer Deposition. *Nature Communications* **2014**, *5*, 3264.

28. Weber, M. J.; Mackus, A. J. M.; Verheijen, M. A.; van der Marel, C.; Kessels, W. M. M., Supported Core/Shell Bimetallic Nanoparticles Synthesis by Atomic Layer Deposition. *Chemistry of Materials* **2012**, *24*, 2973-2977.

29. Ramachandran, R. K.; Dendooven, J.; Filez, M.; Galvita, V. V.; Poelman, H.; Solano, E.; Minjauw, M. M.; Devloo-Casier, K.; Fonda, E.; Hermida-Merino, D.; et al. Atomic Layer Deposition Route To Tailor Nanoalloys of Noble and Non-Noble Metals. *ACS Nano* **2016**, *10*, 8770−8777

30. Ramachandran, R. K.; Filez, M.; Dendooven, J.; Galvita, V. V.; Poelman, H.; Solano, E.; Fonda, E.; Marin, G. B.; Detavernier, C., Size-and Composition-Controlled Pt–Sn Bimetallic Nanoparticles Prepared by Atomic Layer Deposition. *RSC advances* **2017**, *7*, 20201-20205.

31. Cao, Y.-Q.; Zi, T.-Q.; Liu, C.; Cui, D.-P.; Wu, D.; Li, A.-D., Co−Pt Bimetallic Nanoparticles with Tunable Magnetic and Electrocatalytic Properties Prepared by Atomic Layer Deposition. *Chemical Communications* **2020**, *56*, 8675-8678.

32. Wang, S.; Xu, D.; Zhu, D.; Zhao, B.; Guan, H.; Qin, Y.; Wu, B.; Yang, Y.; Li, Y., Elucidating the Restructuring-Induced Highly Active Bimetallic Pt–Co/Kl Catalyst for the Aromatization of N-Heptane. *Chemical Communications* **2020**, *56*, 892-895.

33. Camacho-Bunquin, J.; Ferrandon, M. S.; Sohn, H.; Kropf, A. J.; Yang, C.; Wen, J.; Hackler, R. A.; Liu, C.; Celik, G.; Marshall, C. L.; et al. Atomically Precise Strategy to a Ptzn Alloy Nanocluster Catalyst for the Deep Dehydrogenation of N-Butane to 1, 3-Butadiene. *ACS Catalysis* **2018**, *8*, 10058-10063.

34. Ramachandran, R. K.; Dendooven, J.; Detavernier, C., Controlled Synthesis of Fe-Pt Nanoalloys Using Atomic Layer Deposition. *Nanotechnology* **2020,** *32***,** 095602.

35. Siddiqi, G.; Sun, P.; Galvita, V.; Bell, A. T., Catalyst Performance of Novel Pt/Mg (Ga)(Al) O Catalysts for Alkane Dehydrogenation. *Journal of Catalysis* **2010**, *274*, 200-206.

36. Sun, P.; Siddiqi, G.; Chi, M.; Bell, A. T., Synthesis and Characterization of a New Catalyst Pt/Mg (Ga)(Al) O for Alkane Dehydrogenation. *Journal of Catalysis* **2010**, *274*, 192-199.

37. Filez, M.; Redekop, E. A.; Poelman, H.; Galvita, V. V.; Ramachandran, R. K.; Dendooven, J.; Detavernier, C.; Marin, G. B., Unravelling the Formation of Pt–Ga Alloyed Nanoparticles on Calcined Ga-Modified Hydrotalcites by in Situ Xas. *Chemistry of Materials* **2014**, *26*, 5936-5949.

38. Ota, A.; Kröhnert, J.; Weinberg, G.; Kasatkin, I.; Kunkes, E. L.; Ferri, D.; Girgsdies, F.; Hamilton, N.; Armbrüster, M.; Schlögl, R.; et al. Dynamic Surface Processes of Nanostructured Pd2ga Catalysts Derived from Hydrotalcite-Like Precursors. *ACS Catalysis* **2014**, *4*, 2048-2059.

39. Ota, A.; Armbrüster, M.; Behrens, M.; Rosenthal, D.; Friedrich, M.; Kasatkin, I.;

Girgsdies, F.; Zhang, W.; Wagner, R.; Schlögl, R., Intermetallic Compound Pd2ga as a Selective Catalyst for the Semi-Hydrogenation of Acetylene: From Model to High Performance Systems. *The Journal of Physical Chemistry C* **2011**, *115*, 1368-1374.

40. Väyrynen, K.; Hatanpää, T.; Mattinen, M.; Mizohata, K.; Meinander, K.; Räisänen, J.; Link, J.; Stern, R.; Ritala, M.; Leskelä, M., Atomic Layer Deposition of Intermetallic Co3sn2 and Ni3sn2 Thin Films. *Advanced Materials Interfaces* **2019**, *6*, 1801291.

41. Mullings, M. N.; Hägglund, C.; Bent, S. F., Tin Oxide Atomic Layer Deposition from Tetrakis (Dimethylamino) Tin and Water. *Journal of Vacuum Science & Technology A: Vacuum, Surfaces, and Films* **2013**, *31*, 061503.

42. Ansari, M. Z.; Nandi, D. K.; Janicek, P.; Ansari, S. A.; Ramesh, R.; Cheon, T.; Shong, B.; Kim, S.-H., Low-Temperature Atomic Layer Deposition of Highly Conformal Tin Nitride Thin Films for Energy Storage Devices. *ACS Applied Materials & Interfaces* **2019**, *11*, 43608-43621.

43. Ham, G.; Shin, S.; Park, J.; Choi, H.; Kim, J.; Lee, Y.-A.; Seo, H.; Jeon, H., Tuning the Electronic Structure of Tin Sulfides Grown by Atomic Layer Deposition. *ACS Applied Materials & Interfaces* **2013**, *5*, 8889-8896.

44. Van de Kerckhove, K.; Dendooven, J.; Detavernier, C., Annealing of Thin "Tincone" Films, a Tin-Based Hybrid Material Deposited by Molecular Layer Deposition, in Reducing, Inert, and Oxidizing Atmospheres. *Journal of Vacuum Science & Technology A: Vacuum, Surfaces, and Films* **2018**, *36*, 051506.

45. Barick, B. K.; Simon, A.; Weisbord, I.; Shomrat, N.; Segal-Peretz, T., Tin Oxide Nanostructure Fabrication Via Sequential Infiltration Synthesis in Block Copolymer Thin Films. *Journal of colloid and interface science* **2019**, *557*, 537-545.

46. Xie, Q.; Jiang, Y.-L.; Detavernier, C.; Deduytsche, D.; Van Meirhaeghe, R. L.; Ru, G.-P.; Li, B.-Z.; Qu, X.-P., Atomic Layer Deposition of Ti O 2 from Tetrakis-Dimethyl-Amido Titanium or Ti Isopropoxide Precursors and H 2 O. *Journal of applied physics* **2007**, *102*, 083521.

47. Musschoot, J.; Xie, Q.; Deduytsche, D.; Van den Berghe, S.; Van Meirhaeghe, R.; Detavernier, C., Atomic Layer Deposition of Titanium Nitride from Tdmat Precursor. *Microelectronic Engineering* **2009**, *86*, 72-77.

48. Aaltonen, T.; Ritala, M.; Sajavaara, T.; Keinonen, J.; Leskelä, M., Atomic Layer Deposition of Platinum Thin Films. *Chemistry of materials* **2003**, *15*, 1924-1928.

49. Dendooven, J.; Solano, E.; Minjauw, M. M.; Van de Kerckhove, K.; Coati, A.; Fonda, E.; Portale, G.; Garreau, Y.; Detavernier, C., Mobile Setup for Synchrotron Based in Situ Characterization During Thermal and Plasma-Enhanced Atomic Layer Deposition. *Review of Scientific Instruments* **2016**, *87*, 113905.

50. Renaud, G.; Lazzari, R.; Leroy, F., Probing Surface and Interface Morphology with Grazing Incidence Small Angle X-Ray Scattering. *Surface Science Reports* **2009**, *64*, 255-380.

51. Knaepen, W.; Detavernier, C.; Van Meirhaeghe, R.; Sweet, J. J.; Lavoie, C., In-Situ X-Ray Diffraction Study of Metal Induced Crystallization of Amorphous Silicon. *Thin Solid Films* **2008**, *516*, 4946-4952.

52. Elam, J. W.; Baker, D. A.; Martinson, A. B. F.; Pellin, M. J.; Hupp, J. T., Atomic Layer Deposition of Indium Tin Oxide Thin Films Using Nonhalogenated Precursors. *The Journal of Physical Chemistry C* **2008**, *112*, 1938-1945.

53. Zhu, T.; van Grootel, P. W.; Filot, I. A.; Sun, S.-G.; van Santen, R. A.; Hensen, E. J., Microkinetics of Steam Methane Reforming on Platinum and Rhodium Metal Surfaces. *Journal of catalysis* **2013**, *297*, 227-235.

54. Solano, E.; Dendooven, J.; Ramachandran, R. K.; Van de Kerckhove, K.; Dobbelaere, T.; Hermida-Merino, D.; Detavernier, C., Key Role of Surface Oxidation and Reduction Processes in the Coarsening of Pt Nanoparticles. *Nanoscale* **2017**, *9*, 13159-13170.

55. Filez, M.; Redekop, E. A.; Dendooven, J.; Ramachandran, R. K.; Solano, E.; Olsbye, U.; Weckhuysen, B. M.; Galvita, V. V.; Poelman, H.; Detavernier, C.; et al. Formation and Functioning of Bimetallic Nanocatalysts: The Power of X-Ray Probes. *Angewandte Chemie International Edition* **2019**, *58*, 13220-13230.

56. Sieben, J. M.; Duarte, M. M. E., Nanostructured Pt and Pt–Sn Catalysts Supported on Oxidized Carbon Nanotubes for Ethanol and Ethylene Glycol Electro-Oxidation. *International Journal of Hydrogen Energy* **2011**, *36*, 3313-3321.

57. Switzer, E. E.; Olson, T. S.; Datye, A. K.; Atanassov, P.; Hibbs, M. R.; Cornelius, C. J., Templated Pt–Sn Electrocatalysts for Ethanol, Methanol and Co Oxidation in Alkaline Media. *Electrochimica Acta* **2009**, *54*, 989-995.

58. Bocanegra, S. A.; Guerrero-Ruiz, A.; de Miguel, S. R.; Scelza, O. A., Performance of Ptsn Catalysts Supported on Mal2o4 (M: Mg or Zn) in N-Butane Dehydrogenation: Characterization of the Metallic Phase. *Applied Catalysis A: General* **2004**, *277*, 11-22.

59. Iglesias-Juez, A.; Beale, A. M.; Maaijen, K.; Weng, T. C.; Glatzel, P.; Weckhuysen, B. M., A Combined in Situ Time-Resolved Uv–Vis, Raman and High-Energy Resolution X-Ray Absorption Spectroscopy Study on the Deactivation Behavior of Pt and Ptsn Propane Dehydrogenation Catalysts under Industrial Reaction Conditions. *Journal of Catalysis* **2010**, *276*, 268-279.

60. Zhu, H.; Anjum, D. H.; Wang, Q.; Abou-Hamad, E.; Emsley, L.; Dong, H.; Laveille, P.; Li, L.; Samal, A. K.; Basset, J.-M., Sn Surface-Enriched Pt–Sn Bimetallic Nanoparticles as a Selective and Stable Catalyst for Propane Dehydrogenation. *Journal of catalysis* **2014**, *320*, 52-62.

61. Van Herpen, M.; Klunder, D.; Soer, W.; Moors, R.; Banine, V., Sn Etching with Hydrogen Radicals to Clean Euv Optics. *Chemical Physics Letters* **2010**, *484*, 197-199.

62. Faradzhev, N.; Sidorkin, V., Hydrogen Mediated Transport of Sn to Ru Film Surface. *Journal of Vacuum Science & Technology A: Vacuum, Surfaces, and Films* **2009**, *27*, 306-314.

63. Soer, W.; van Herpen, M.; Jak, M.; Gawlitza, P.; Braun, S.; Salashchenko, N.; Banine, V., Atomic-Hydrogen Cleaning of Sn from Mo/Si and Dlc/Si Extreme Ultraviolet Multilayer Mirrors. *Journal of Micro/Nanolithography, MEMS, and MOEMS* **2012**, *11*, 021118.

64. Pike, S. D.; White, E. R.; Regoutz, A.; Sammy, N.; Payne, D. J.; Williams, C. K.; Shaffer, M. S. P., Reversible Redox Cycling of Well-Defined, Ultrasmall Cu/Cu2o Nanoparticles. *ACS Nano* **2017**, *11*, 2714-2723.

65. Bordet, A.; Lacroix, L. M.; Soulantica, K.; Chaudret, B., A New Approach to the Mechanism of Fischer–Tropsch Syntheses Arising from Gas Phase Nmr and Mass Spectrometry. *ChemCatChem* **2016**, *8*, 1727-1731.

66. Qin, X.; Zaera, F., Chemistry of Ruthenium Diketonate Atomic Layer Deposition (Ald) Precursors on Metal Surfaces. *The Journal of Physical Chemistry C* **2018**, *122*, 13481-13491.

TOC Graphic

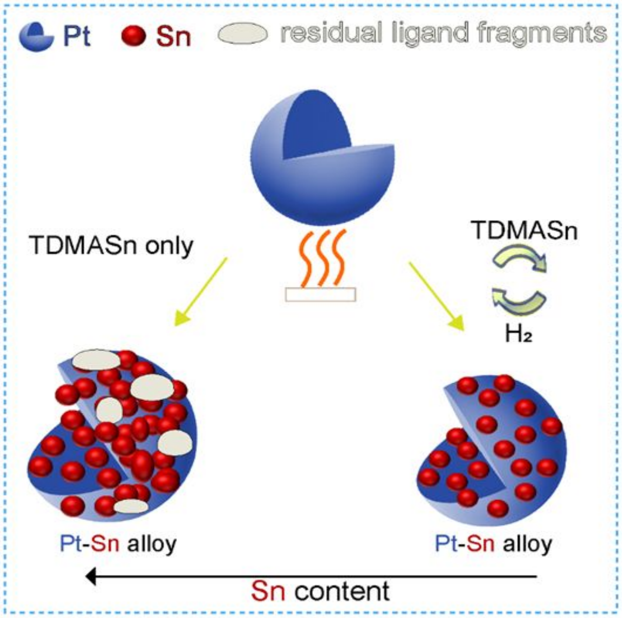
Pt
Sn
residual ligand fragments
TDMASn only
TDMASn
H_2
Pt-Sn alloy
Pt-Sn alloy
Sn content